Viscous Effects on Transonic Airfoil Stability and Response

H. M. Berry*
General Dynamics Corporation, Ft. Worth, Texas
J. T. Batina†
NASA Langley Research Center, Hampton, Virginia
and
T. Y. Yang‡
Purdue University, West Lafayette, Indiana

Viscous effects on transonic airfoil stability and response are investigated using an integral boundary-layer model coupled to the inviscid XTRAN2L transonic small-disturbance code. The unsteady transonic airloads required for stability analyses are computed using a pulse transfer function analysis including viscous effects. The pulse analysis provides unsteady aerodynamic forces for a wide range of reduced frequency in a single flowfield computation. Nonlinear time-marching aeroelastic solutions are presented that show the effects of viscosity on airfoil response behavior and flutter. A state-space aeroelastic model employing Padé approximants to describe the unsteady airloads is used to study the effects of viscosity on transonic airfoil stability. State-space dynamic pressure root-loci are in good overall agreement with time-marching damping and frequency estimates. Parallel sets of results with and without viscous effects reveal the effects of viscosity on transonic unsteady airloads and aeroelastic characteristics of airfoils.

Nomenclature

a_h = nondimensional distance from midchord to elastic axis
b = airfoil semichord
c = airfoil chord
c_{ℓ_h} = lift coefficient due to plunge
c_{ℓ_α} = lift coefficient due to pitch
c_{m_h} = moment coefficient about pitching axis due to plunge
c_{m_α} = moment coefficient about pitching axis due to pitch
C_p = pressure coefficient
C_p^* = critical pressure coefficient
h = nondimensional plunge displacement, positive downward from elastic axis
h_0 = dynamic plunge amplitude
k = $\omega b/U$, reduced frequency
m = airfoil mass per unit span
M = freestream Mach number
Q = $(1/\mu)(U/b\omega_\alpha)^2$, nondimensional dynamic pressure
Q_F = $(1/\mu)(U_F/b\omega_\alpha)^2$, nondimensional flutter dynamic pressure
r_α = airfoil radius of gyration about elastic axis
Re = Uc/ν, Reynolds number
s = $\sigma + i\omega$, Laplace transform variable
t = time, s
$\bar{t}$ = $\omega_\alpha t$, nondimensional time
U = freestream velocity
U_F = flutter speed
x = distance aft of leading edge
x_α = nondimensional distance from elastic axis to mass center
α = airfoil angle of attack, positive leading edge up
α_m = airfoil mean angle of attack
α_0 = airfoil dynamic pitch amplitude
μ = $m/\pi\rho b^2$, airfoil mass ratio
ν = kinematic viscosity
ρ = freestream air density
τ = Ut/b, nondimensional time
ω = angular frequency
ω_F = flutter frequency
ω_h = uncoupled plunge natural frequency
ω_α = uncoupled pitch natural frequency

Received Jan. 2, 1985; presented as Paper 85-0586 at the AIAA/ASME/ASCE/AHS 26th Structures, Structural Dynamics and Materials Conference, Orlando, FL, April 15-17, 1985; revision received Jan. 15, 1986.

*Engineer, Structural Dynamics Group, Ft. Worth Division. Member AIAA.
†Research Scientist, Unsteady Aerodynamics Branch, Loads and Aeroelasticity Division. Member AIAA.
‡Professor and Dean, Schools of Engineering. Fellow AIAA.

Introduction

RESEARCH directed at a better understanding of aerodynamic and aeroelastic phenomena at transonic speeds has increased greatly in recent years. These developments have been made possible by the advances made in computer power and numerical solution techniques.[1] Much effort has been put into the development of accurate yet cost-efficient methods of calculating unsteady transonic airloads, as well as the prediction of aeroelastic characteristics such as flutter and divergence.

Solutions for inviscid unsteady transonic flowfields about oscillating airfoils have been made possible using computer codes such as LTRAN2.[2] While the inviscid flowfields predicted by LTRAN2 give valid results for many cases, these solutions are not adequate when viscous effects are important. Rizzetta[3] incorporated the effects of viscosity into the LTRAN2 code using a viscous ramp and Green's lag-entrainment equations, an integral boundary-layer model. Guruswamy and Goorjian[4] applied this modified version of LTRAN2 to investigate the effects of viscosity on transonic aerodynamic and aeroelastic characteristics of oscillating airfoils. As many as 8000 time steps per cycle of oscillatory motion were required in the viscous lag-entrainment calculations to obtain reasonably converged results. Steady and unsteady viscous results agreed better with experiment than did comparable inviscid solutions.

Houwink[5] developed a procedure for an explicit coupling of the unsteady transonic flow and turbulent boundary-layer computations and incorporated them into the LTRAN2-NLR[6] code. Satisfactorily converged results were obtained in as few as 120 time steps per cycle using the resulting LTRANV[5] code. More recently, Howlett[7] has modified the viscous coupling procedure of Rizzetta for application to the XTRAN2L[8] general-frequency transonic small-disturbance code. Iteration of an explicitly coupled viscous boundary-layer solution with the inviscid outer flow at each time step provides converged flowfield solutions in as few as 1 or 2 iterations with 360 time steps per cycle. Viscous solutions are obtained in computer times approximately twice that of the comparable inviscid solution. Therefore, a more practical and affordable assessment of the effects of viscosity on transonic unsteady aerodynamic forces and aeroelastic characteristics of oscillating airfoils is now possible. The explicitly coupled viscous-inviscid procedure of Ref. 7 is used in the present study to calculate time-marching flutter solutions and transonic unsteady airloads required for aeroelastic stability analyses.

The purpose of this paper is to investigate further the effects of viscosity on transonic airfoil stability and response. The objectives of the study were: 1) to investigate application of the pulse transfer-function analysis of Seidel et al.[9] to treat airloads including viscous effects; 2) to investigate application of the nonlinear time-marching flutter solution procedure of Edwards et al.[10] to transonic airfoil response including viscous effects; 3) to assess the accuracy of state-space aeroelastic modeling to predict airfoil stability including viscous effects by comparison with time-marching analyses; and 4) to apply state-space modeling to study the effects of viscosity on transonic airfoil stability. Parallel sets of results are presented with and without viscous effects to determine the effects of viscosity on transonic airfoil stability and response.

Computational Procedures

XTRAN2L Transonic Code

The finite-difference code XTRAN2L solves the transonic small-disturbance potential equation and thus provides predictions of unsteady transonic flowfields about oscillating airfoils. The inviscid algorithm, however, tends to overpredict the shock strength and locates the shock too far aft for cases where viscous effects are important. The effects of viscosity are accounted for by coupling an integral boundary layer to the inviscid potential outer flow in a quasisteady fashion.[7] In these calculations, Green's lag-entrainment equations are integrated along the airfoil from a transition point selected at 10% chord to the downstream boundary. Iteration of the viscous-inviscid solution may be performed, thus ensuring converged flowfield results at each time step.

Pulse Transfer-Function Analysis

Unsteady aerodynamic forces required for stability calculations are computed using the pulse transfer-function analysis available in XTRAN2L. This analysis is based on the assumption that the unsteady forces are locally linear about the nonlinear transonic mean flow. In the pulse analysis, the airfoil is given a small prescribed pulse in a given mode of motion and the aerodynamic transients are calculated. For pitch motion, the pulse is given by

$$\alpha = \alpha_m + \alpha_0 e^{-(\tau - 17.5\Delta\tau)^2} \tag{1}$$

where $\Delta\tau$ is the nondimensional time step. A similar expression describes the pulse for plunge motion. The unsteady aerodynamic transfer-function is then determined by dividing a fast Fourier transform (FFT) of the output force time history by the FFT of the input pulse motion. The pulse analysis provides unsteady aerodynamic forces for a wide range of reduced frequency in a single flowfield computation. This is in contrast to multiple flowfield computations required for calculating oscillatory forces for discrete frequencies. A typical inviscid pulse analysis was computed with $\Delta\tau = 5\pi/32$ and 1024 time steps, while a typical viscous pulse analysis was computed with $\Delta\tau = 2\pi/27$ and 2160 time steps.

Time-Marching Aeroelastic Analysis

The aeroelastic system considered consists of plunge and pitch degrees of freedom. The structural equations of motion are coupled with the aerodynamic solution procedure of XTRAN2L for simultaneous time-integration. These equations are numerically integrated in time using the modified state-transition matrix integrator of Edwards et al.[10] A typical inviscid analysis was performed with $\Delta t = 0.0004$ and a typical viscous solution was obtained with $\Delta t = 0.0003$. In general, several aeroelastic transients were calculated for a range of nondimensional dynamic pressure Q. Values of Q were selected that resulted in subcritical damped responses and supercritical diverging responses. The nondimensional flutter dynamic pressure Q_F was calculated by interpolation and then confirmed by obtaining neutrally stable responses.

Damping and frequency of the aeroelastic modes are estimated from the transient response curves using the method of Bennett and Desmarais.[11] These modal estimates are determined by a least squares curve-fit of the aeroelastic transients using complex exponential functions of the form

$$X(t) = a_0 + \sum_{j=1}^{m} e^{(\sigma/\omega_\alpha)_j \bar{t}} \left[a_j \cos\left(\frac{\omega}{\omega_\alpha}\right)_j \bar{t} + b_j \sin\left(\frac{\omega}{\omega_\alpha}\right)_j \bar{t} \right] \tag{2}$$

Damping and frequency estimates from the time-marching analysis are plotted in the complex s-plane.

Padé Model Stability Analysis

Aeroelastic stability analyses are performed using a state-space aeroelastic model, termed the Padé model, similar to that of Refs. 12 and 13. The locally linear Padé model provides a relatively inexpensive determination of airfoil stability, while retaining the nonlinear properties of the transonic mean flow. The Padé model is derived by assuming a linear superposition of airloads due to airfoil plunge and pitch motions. The required airloads are approximated by curvefitting the XTRAN2L unsteady aerodynamic forces with a Padé approximating function.[12] The function may then be rewritten as a set of ordinary differential equations which, when coupled to the equations of motion and Laplace transformed, leads to a linear first-order matrix equation

$$(s/\omega_\alpha)\{z\} = [A]\{z\} \tag{3}$$

where $\{z\}$ contains the displacements, velocities, and augmented states and $[A]$ is a real matrix of constant elements. Equation (3) is solved using linear eigenvalue solution techniques for specified values of Q. The resulting eigenvalues are plotted in a dynamic pressure "root-locus" type format and are compared with time-marching damping and frequency estimates in the complex s-plane.

Results and Discussion

Calculations were performed for the NACA 64A010 Ames (herein referred to as NACA 64A010A) and the MBB-A3 airfoils. The airfoil coordinates required for aerodynamic computations were taken from Ref. 14. The computational conditions were selected to match the experimental conditions reported in Refs. 15 and 16, as listed in Table 1. Aeroelastic results are presented for two example sets of structural parameter values. Example 1 is Case A of Isogai,[17] which has normal modes similar to those of a streamwise section near the tip of a swept-back wing. The wind-off coupled plunge

and pitch frequencies are 71.34 and 533.8 rad/s, respectively. The pivotal point for the plunge mode is located 1.44 chordlengths ahead of the leading edge. The pivotal point for the pitch mode is 0.068 chordlengths forward of midchord. Example 2 is the structural configuration used by Edwards et al.[10] (also termed Example 2 in Ref. 10), which has normal mode frequencies that are close together. The wind-off coupled plunge and pitch frequencies are 23.5 and 35.0 rad/s, respectively. Values for the structural parameters for the two examples are listed in Table 2.

Transonic Steady Aerodynamic Results

Steady flowfields were computed for use as initial conditions for unsteady aerodynamic calculations. Steady pressure distributions for the lower surface of the NACA 64A010A airfoil are shown in Fig. 1 along with a plot of the airfoil contour. Both inviscid and viscous XTRAN2L pressure distributions are presented and compared with the experimental data of Davis.[15] Calculations were performed at the experimental conditions[15] of $M=0.796$, $\alpha_m=-0.21$ deg, and $Re=12.56\times10^6$, which are herein termed Computational Condition 1 (see Table 1). All three sets of results are in reasonable agreement. In the region of the shock, the viscous computations are in better agreement with the experimental data than the inviscid computations. The viscous effects are relatively mild for this case.

Steady pressure distributions for the MBB-A3 airfoil are shown in Fig. 2 along with a plot of the airfoil contour. Computational results were obtained at two different sets of conditions for comparison with the experimental data of Bucciantini et al.[16] The first set corresponds to the uncorrected tunnel conditions[16] of $M=0.765$, $\alpha_m=1.5$ deg, and $Re=6.0\times10^6$, which are herein termed Computational Condition 2, as listed in Table 1. The second set corresponds to the theoretical design condition[16] of $M=0.7557$ and $\alpha_m=1.3$ deg, which is herein termed Computational Condition 3, as listed in Table 1. Computational Condition 3 allows inviscid computations to match the experimental pressure data[16] and hence viscous calculations are not presented at this condition. Both inviscid and viscous solutions are presented at Computational Condition 2. As shown in Fig. 2, all four sets of results agree well along the lower surface of the airfoil except near the leading edge. For the upper surface, the XTRAN2L pressure distributions at Computational Condition 2 indicate an overprediction of the shock strength and location, although the viscous computation is in slightly better agreement with experimental data than the inviscid computation. Differences between the viscous results and experiment may be attributed to the fact that the boundary layer model does not account for the strong interaction between the shock wave and the boundary layer. Inviscid calculations performed at Computational Condition 3, however, show much better agreement with experiment than either of the calculations performed at Computational Condition 2.

Table 1 Airfoils and computational conditions for transonic aerodynamic and aeroelastic analyses

Airfoil	Computational Condition	M	α_m, deg	Re
NACA 64A010A	1	0.796	−0.21	12.56×10^6
MBB-A3	2	0.765	1.50	6.0×10^6
MBB-A3	3	0.7557	1.30	

Table 2 Structural parameter values for aeroelastic analyses

Structural parameter	Example 1	Example 2
a_h	−2.0	−0.042
x_α	1.8	−0.036
r_α	1.865	1.368
μ	60.0	60.0
ω_h	100.0	23.5
ω_α	100.0	35.0

Transonic Unsteady Aerodynamic Results

Unsteady aerodynamic forces required for Padé model stability calculations were computed using the pulse transfer-function analysis. Representative results for the lift coefficient due to pitch, c_{l_α}, are plotted in Fig. 3 as a function of reduced frequency k. These results were obtained using the pulse analysis with viscous effects for the NACA 64A010A airfoil at Computational Condition 1 and a small pulse amplitude of $\alpha_0=0.1$ deg. To assess the accuracy of the pulse analysis, oscillatory calculations including the effects of viscosity were performed for comparison. Results were obtained using an amplitude of $\alpha_0=0.1$ deg at eight values of reduced frequency $k=0.05$, 0.1, 0.2, 0.4, 0.8, 1.2, 1.6,

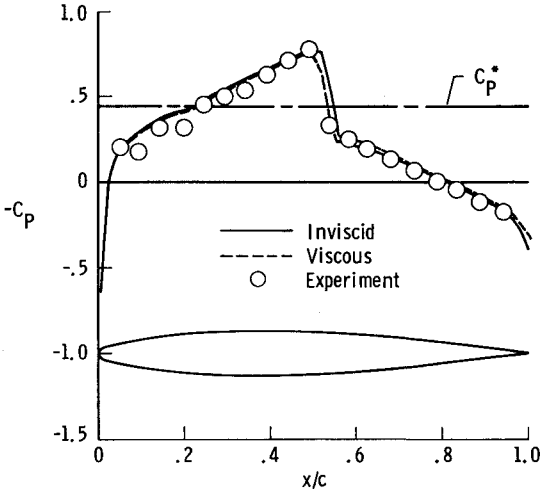

Fig. 1 Steady pressure distributions for the lower surface of the NACA 64A010A airfoil at $M=0.796$ and $\alpha_m=-0.21$ deg.

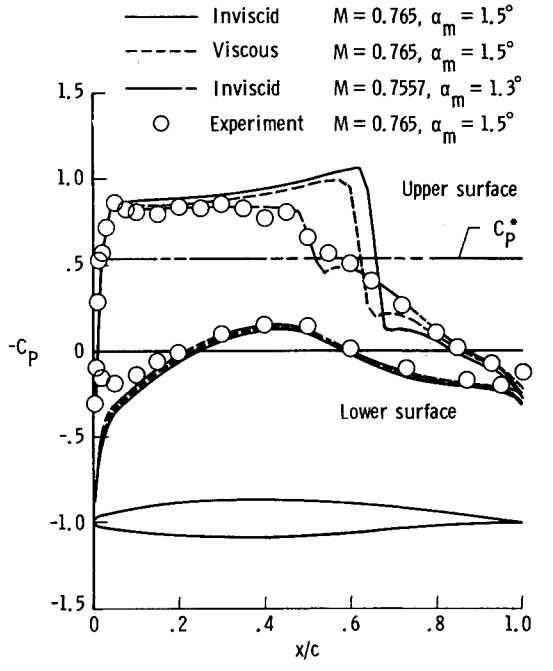

Fig. 2 Steady pressure distributions for the MBB-A3 airfoil at $M=0.765$, $\alpha_m=1.5$ deg and $M=0.7557$, $\alpha_m=1.3$ deg.

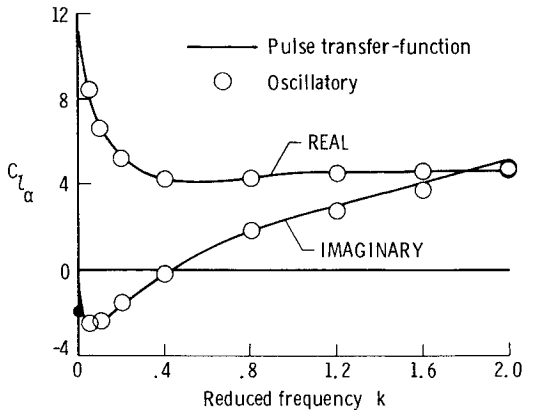

Fig. 3 Lift coefficient due to pitch about the quarter chord, c_{ℓ_α}, calculated using pulse and oscillatory analyses with viscous effects, for the NACA 64A010A airfoil at $M=0.796$, $\alpha_m=-0.21$ deg, and $\alpha_0=0.1$ deg.

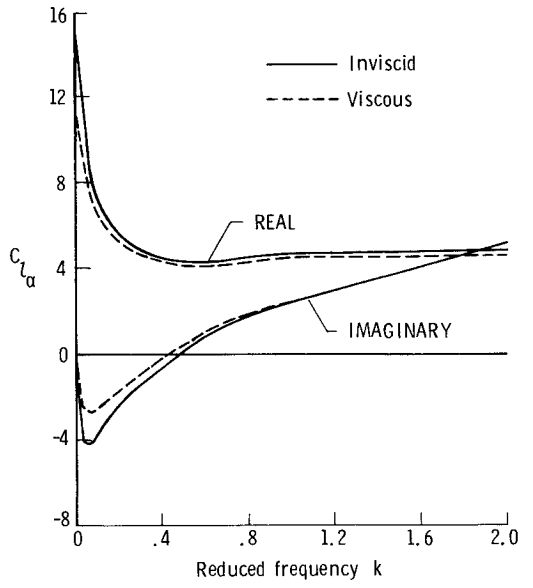

Fig. 4 Comparison of inviscid and viscous pulse results for the lift coefficient due to pitch about the quarter chord, c_{ℓ_α}, for the NACA 64A010A airfoil at $M=0.796$, $\alpha_m=-0.21$ deg, and $\alpha_0=0.1$ deg.

and 2.0. Three cycles of oscillatory motion with 360 time steps per cycle and 1 viscous iteration per time step were used for most cases. For $k=0.05$, however, 720 time steps per cycle and 2 viscous iterations per time step were required. As shown in Fig. 3, the pulse transfer-function is in excellent agreement with the oscillatory airloads. The excellent agreement between the two sets of results for this representative case clearly demonstrates the applicability of the pulse transfer-function analysis to include viscous effects.

To investigate the effects of viscosity on transonic unsteady airloads, inviscid and viscous pulse analyses were performed. A representative comparison between pulse results for c_{ℓ_α} is given in Fig. 4 for the NACA 64A010A airfoil (at Computational Condition 1). Both sets of results were computed using a pulse amplitude of 0.1 deg. The inviscid and viscous pulse results show the same trends with respect to reduced frequency. Differences between the inviscid and viscous c_{ℓ_α} results are largest for low values of k. In the low k range, viscosity decreased the magnitude of both the real and imaginary parts.

The effects of pulse amplitude on transonic unsteady airloads were investigated by obtaining unsteady forces for successively increased pulse amplitudes. The inviscid pulse amplitude computations (not shown here) indicate that the unsteady forces are relatively independent of amplitude. Viscous pulse amplitude computations showing effects of amplitude for c_{ℓ_α} are presented in Fig. 5 for the NACA 64A010A airfoil (at Computational Condition 1). Comparison between viscous pulse computations at $\alpha_0=0.1$ deg with the computations at $\alpha_0=1.0$ deg shows small differences over the range of k plotted. With increased pulse amplitude, the magnitudes of both the real and imaginary parts of c_{ℓ_α} are increased. Recent improvements to the boundary-layer model made by Howlett[20] indicate that these viscous pulse amplitude effects may be spurious. The most accurate results are therefore believed to be the calculations performed at $\alpha_0=0.1$ deg.

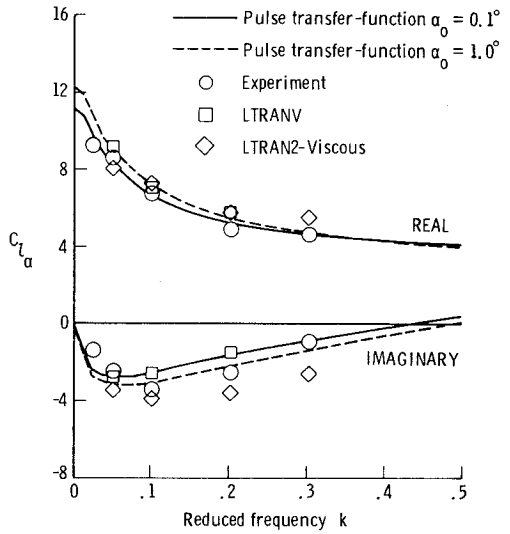

Fig. 5 Comparison of pulse results with experimental data, LTRANV, and LTRAN2-Viscous results for the lift coefficient due to pitch about the quarter chord, c_{ℓ_α}, for the NACA 64A010A airfoil at $M=0.796$ and $\alpha_m=-0.21$ deg.

Unsteady experimental data from Davis[15] and the computational results of Houwink[18] and Guruswamy and Goorjian[4] are also plotted in Fig. 5 for further comparison. The experimental data of Ref. 15 was obtained using a harmonic pitch amplitude of $\alpha_0\approx 1.0$ deg. The unsteady forces of Ref. 18 were calculated with LTRANV code using $\alpha_0=1.0$ deg, $M=0.8$, and $\alpha_m=0$ deg. The unsteady forces of Ref. 4 were calculated with the viscous version of LTRAN2 at Computational Condition 1 using harmonic pitch amplitudes selected to match the experiment. As shown in Fig. 5, the viscous pulse computations performed using $\alpha_0=0.1$ deg show good overall agreement with the experimental forces, except for the imaginary values of c_{ℓ_α} at $k=0.1$ and 0.2. Comparison of the viscous pulse computations with the LTRANV airloads shows good overall agreement. Comparison of the viscous LTRAN2 results for c_{ℓ_α} with all of the other unsteady forces presented in Fig. 5 shows good general agreement in the real part, although the imaginary part is consistently overpredicted.

Time-Marching Aeroelastic Results

Time-marching calculations were first performed using a small initial plunge displacement of $h(0)=0.001$ to determine the value of Q resulting in neutrally stable aeroelastic transients. The effects of amplitude on flutter were then investigated by obtaining time-marching responses for successively increased initial plunge displacement $h(0)$. In these calculations, the dynamic pressure Q was set equal to the flutter dynamic pressure Q_F previously determined using $h(0)=0.001$. Only representative responses for the NACA 64A010A airfoil (at Computational Condition 1) are pre-

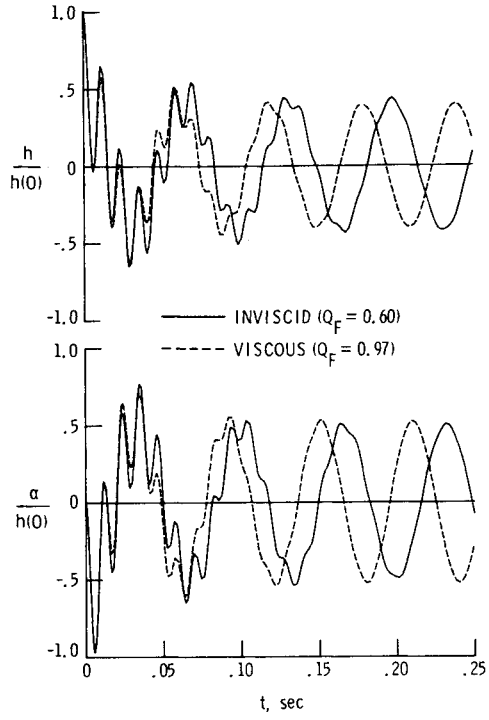

Fig. 6 NACA 64A010A neutrally stable time-marching response histories of Example 1 at $M=0.796$ and $\alpha_m=-0.21$ deg.

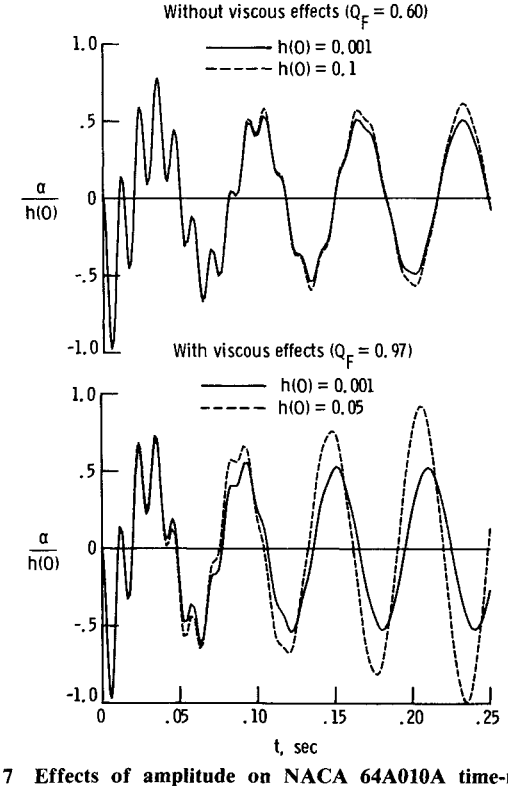

Fig. 7 Effects of amplitude on NACA 64A010A time-marching flutter solutions of Example 1 at $M=0.796$ and $\alpha_m=-0.21$ deg.

sented in this section for the two example sets of structural parameter values listed in Table 2.

Example 1

Neutrally stable plunge and pitch time-marching response histories are presented in Fig. 6. The responses have been normalized by the initial plunge displacement $h(0)=0.001$. Inviscid and viscous flutter dynamic pressure values used to calculate the aeroelastic transients are $Q_F=0.60$ and 0.97, respectively. The responses are bending dominated and are of constant amplitude after the higher-frequency torsion mode transients, visible in the first two to three cycles of motion, have damped out. As shown in Fig. 6, the viscous responses have the same characteristics as the inviscid responses including nearly identical amplitudes. Damping and frequency estimates of the inviscid and viscous aeroelastic transients are plotted in the complex s-plane and are discussed in the following section.

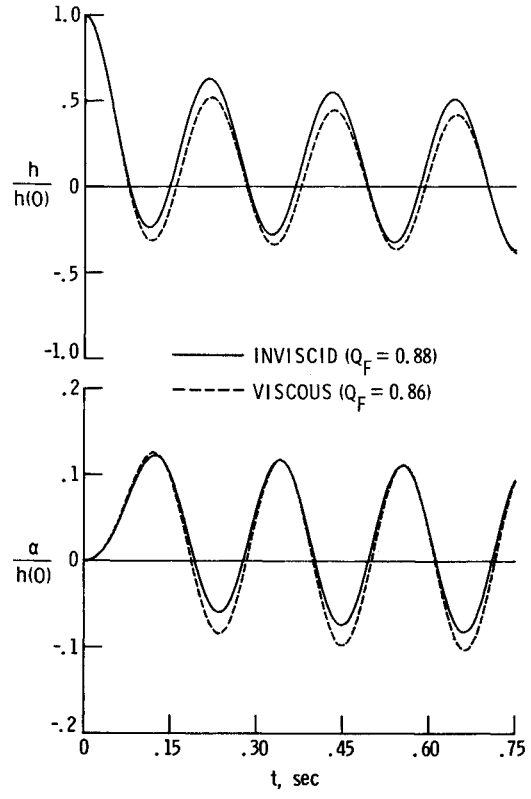

Fig. 8 NACA 64A010A neutrally stable time-marching response histories of Example 2 at $M=0.796$ and $\alpha_m=-0.21$ deg.

The effects of amplitude on the inviscid and viscous time-marching flutter solutions of Fig. 6 are shown in Fig. 7. Plunge and pitch degrees-of-freedom exhibit similar characteristics and hence only the pitch responses are shown. Furthermore, the pitch responses have been normalized by $h(0)$ to allow for direct comparison between amplitude results. The pitch results for $h(0)=0.001$ in Fig. 7 are identical to those of Fig. 6. As shown in the top part of Fig. 7, the inviscid pitch responses become slightly divergent when the initial plunge displacement is increased by a factor of 100. The amplitude effect is consistent with similar results reported in Ref. 10, where increased amplitude had a small destabilizing effect on the flutter responses of the NACA 64A010A and MBB-A3 airfoils for the structural parameter values of Example 1. As shown in the bottom part of Fig. 7, the viscous pitch responses show a similar, but larger, diverging trend for $h(0)=0.05$. At $h(0)=0.1$, viscous responses diverged rapidly and led to program failure. The inviscid pitch responses of Fig. 7 show a weak dependence on amplitude while the responses for the viscous case show a strong amplitude dependence.

Example 2

Neutrally stable time-response histories for the structural parameter values of Example 2 are presented in Fig. 8. These responses are of constant amplitude and oscillate about an exponentially decaying mean. In contrast with Example 1, the inviscid and viscous flutter dynamic pressures are very close, $Q_F=0.88$ and 0.86, respectively. The inviscid and

viscous plunge response histories have approximately the same amplitude and frequency, although the viscous response oscillates about a slightly different mean than the inviscid response. Similar trends are visible in the pitch responses of Fig. 8 (which are of smaller amplitude in comparison with the pitch responses of Example 1 in Fig. 6). In contrast with the responses of Example 1, the higher-frequency transient is not present in the responses of Example 2. The higher-frequency mode is highly damped and thus has a negligible contribution to the total response.

The effects of amplitude on the NACA 64A010A time-marching flutter solutions (at Computational Condition 1) are shown in Fig. 9. Inviscid pitch time-responses that are neutrally stable at $h(0)=0.001$ remain neutrally stable at $h(0)=0.1$. Viscous pitch responses also remain neutrally stable when the initial plunge displacement is increased by a factor of 100. In contrast with the Example 1 responses of Fig. 7, the Example 2 responses of Fig. 9 indicate that the flutter solution is relatively independent of amplitude.

Padé Model Stability Results

Padé model stability calculations were performed using transonic unsteady airloads determined by both inviscid and viscous pulse analyses. Pulse amplitudes were $h_0=0.001$ and $\alpha_0=0.1$ deg. Results for the NACA 64A010A and MBB-A3 airfoils are presented in this section for the two example sets of structural parameter values listed in Table 2. Comparisons between time-marching and Padé model flutter solutions are presented in Table 3.

Example 1

Padé model dynamic pressure root-loci for the NACA 64A010A airfoil (at Computational Condition 1) are shown in the left-half of Fig. 10 for the critical flutter mode only. These root-loci are bending dominated and give the flutter solution by the $\sigma=0$ crossing. The inclusion of viscous effects increased damping in the bending mode and had a negligible effect on the torsion mode (not shown here). Time-marching damping and frequency estimates are plotted in Fig. 10 for $Q=0.4$, 0.8, and 1.2. As shown in the figure, the Padé model root-loci are in good agreement with the time-marching modal estimates in both the inviscid and viscous cases. The Padé model flutter dynamic pressure values are $Q_F=0.62$ and 1.00 for the inviscid and viscous calculations, respectively. Thus, viscous effects increased Q_F by approximately 61%. The Padé model Q_F values are within 3% of the small-amplitude time-marching values presented in the previous section.

Padé model dynamic pressure root-loci for the MBB-A3 airfoil at Computational Conditions 2 and 3 are also shown in Fig. 10. Time-marching modal estimates are plotted for $Q=0.2$, 0.4, 0.6, and 0.8. Padé model results are in good overall agreement with time-marching damping and frequency values. The three sets of computations performed for the MBB-A3 airfoil resulted in steady shock locations of 63%, 61%, and 51% chord and monotonically decreased shock strength as shown in the steady pressure distributions of Fig. 2. The corresponding Padé model flutter dynamic pressure values are $Q_F=0.25$, 0.55, and 0.74, respectively, as listed in Table 3. With successively decreased shock strength and forward shock displacement, there is a monotonic increase in Q_F. At Computational Condition 2, the inclusion of viscous effects increased the flutter dynamic pressure by approximately 124% in comparison with the inviscid result. In the inviscid calculations performed at Computational Condition 3, the small decreases in Mach number and mean angle of attack resulted in a larger increase in damping in the bending root-locus in comparison with that which occurred with the inclusion of viscous effects at Computational Condition 2. The aeroelastic results of Computational Condition 3 are believed to be the most accurate since the inviscid steady pressure calculations for this case agree best with the experimental data in comparison with the other two sets of calculations (as shown in Fig. 2). No experimental flutter data are available for comparison purposes. Corresponding time-marching flutter dynamic pressure values for these three cases are $Q_F=0.27$, 0.46, and 0.65, respectively, as listed in Table 3. Padé model Q_F values for the MBB-A3 airfoil were typically nonconservative for Example 1, which may be at-

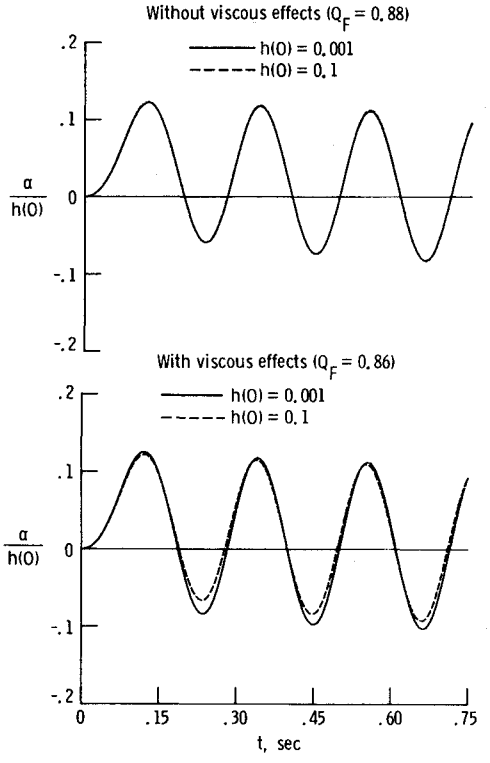

Fig. 9 Effects of amplitude on NACA 64A010A time-marching flutter solutions of Example 2 at $M=0.796$ and $\alpha_m=-0.21$ deg.

Table 3 Comparisons between inviscid and viscous time-marching and Padé model flutter solutions

Airfoils and Computational Conditions	Example	Inviscid				Viscous			
		Time-marching		Padé model		Time-marching		Padé model	
		Q_F	ω_F/ω_α	Q_F	ω_F/ω_α	Q_F	ω_F/ω_α	Q_F	ω_F/ω_α
NACA 64A010A									
$M=0.796$, $\alpha_m=-0.21$ deg	1	0.60	0.96	0.62	0.96	0.97	1.06	1.00	1.06
$Re=12.56\times10^6$	2	0.88	0.84	0.97	0.83	0.86	0.84	0.92	0.83
MBB-A3									
$M=0.765$, $\alpha_m=1.5$ deg	1	0.27	0.82	0.25	0.81	0.46	0.89	0.55	0.92
$Re=6.0\times10^6$	2	0.61	0.94	0.58	0.95	0.86	0.89	0.96	0.80
MBB-A3	1	0.65	0.97	0.74	1.00				
$M=0.7557$, $\alpha_m=1.3$ deg	2	0.76	0.83	0.76	0.83				

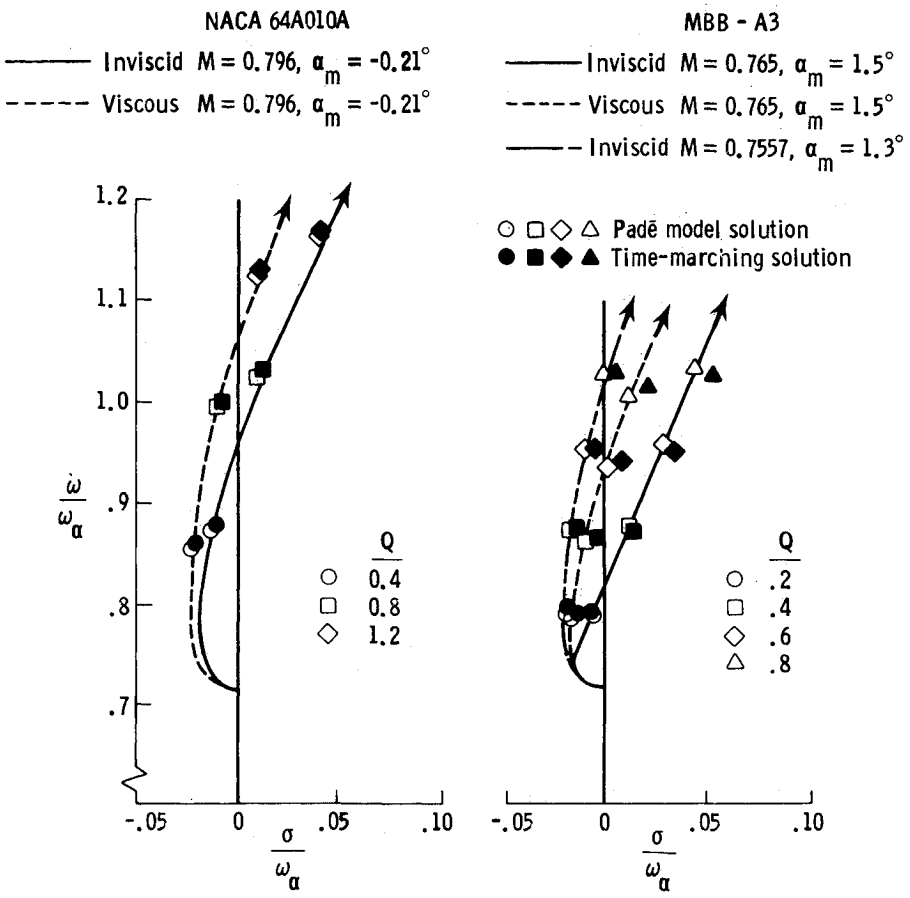

Fig. 10 Effects of viscosity on Padé model and time-marching dynamic pressure root-loci of Example 1.

tributed to the pulse amplitude effects on viscous transonic unsteady airloads (similar to that shown in Fig. 5) and to the amplitude dependence of the flutter responses of Example 1 shown for the NACA 64A010A airfoil in Fig. 7. The larger differences between Padé model and time-marching Q_F values in the viscous case may also be attributed to the more computationally sensitive nature of the viscous XTRAN2L calculations in contrast with the relatively routine inviscid calculations.

The MBB-A3 root-loci are very similar to the NACA 64A010A root-loci, as shown in Fig. 10. The inviscid flutter characteristics of these two airfoils were shown by Bland and Edwards[19] to be nearly identical when the steady shock strengths and locations were matched. The large differences in Q_F between the two airfoils presented here may therefore be attributed to differences in steady shock strength and locations as shown by comparison of Figs. 1 and 2. Also, since the shock on the MBB-A3 airfoil (Computational Condition 2, Fig. 2) is stronger in comparison with the shock on the NACA 64A010A airfoil (Fig. 1), viscosity has more influence on the steady pressures and hence larger changes in Q_F result.

Example 2

Inviscid and viscous Padé model dynamic pressure root-loci for the NACA 64A010A airfoil (at Computational Condition 1) are shown in the left-half of Fig. 11. The inclusion of viscous effects increased damping in the lower-frequency mode and decreased damping in the higher-frequency mode. A switch in modal origin of the flutter mode occurs for this case with the addition of viscosity. The viscous computations give a flutter dynamic pressure value of $Q_F = 0.92$, which is slightly less than the value of $Q_F = 0.97$ given by the inviscid computations. The inviscid Padé model flutter dynamic pressure is within 10% of the time-marching flutter dynamic pressure, $Q_F = 0.88$. Viscous Padé model and time-marching flutter dynamic pressures differ by only 7%, as listed in Table 3. The Padé model root-locus results are in qualitative agreement with the time-marching results. Damping and frequency estimates from the time-marching transients were not obtained, however, because of the closeness in frequency of the two aeroelastic modes.

Padé model dynamic pressure root-loci for the MBB-A3 airfoil are also shown in Fig. 11. The inclusion of viscous effects at Computational Condition 2 increased damping and decreased frequency in the higher-frequency mode. The lower-frequency mode shows only small changes as a result of including viscosity. Dynamic pressures at flutter are $Q_F = 0.58$ and 0.96 for the inviscid and viscous cases, respectively. Padé model Q_F values differ from the small-amplitude time-marching Q_F values listed in Table 3 by 5 and 12% for the inviscid and viscous calculations, respectively. The inclusion of viscous effects resulted in a 66% increase in flutter dynamic pressure, which is in contrast with the small changes in Q_F found for the NACA 64A010A airfoil. The large increase in Q_F between inviscid and viscous MBB-A3 cases at Computational Condition 2 is due to the stronger steady shock in comparison with that of the NACA 64A010A airfoil. A change in the modal origin of the flutter mode occurs, which is opposite to that for the NACA 64A010A airfoil of Example 2 with the inclusion of viscous effects. The inviscid flutter dynamic pressure at Computational Condition 3 is $Q_F = 0.76$, which is the same as the time-marching Q_F value listed in Table 3. The small decreases in Mach number and mean angle of attack in the inviscid calculations result in decreased damping in the lower-frequency mode and increased damping in the higher-frequency mode. The aeroelastic results obtained at Computational Condition 3 are the most accurate since the steady pressures are in closest agreement with the experimental data. Padé model flutter dynamic pressure values for Example 2 were typically nonconservative, which was similar to that found for Example 1.

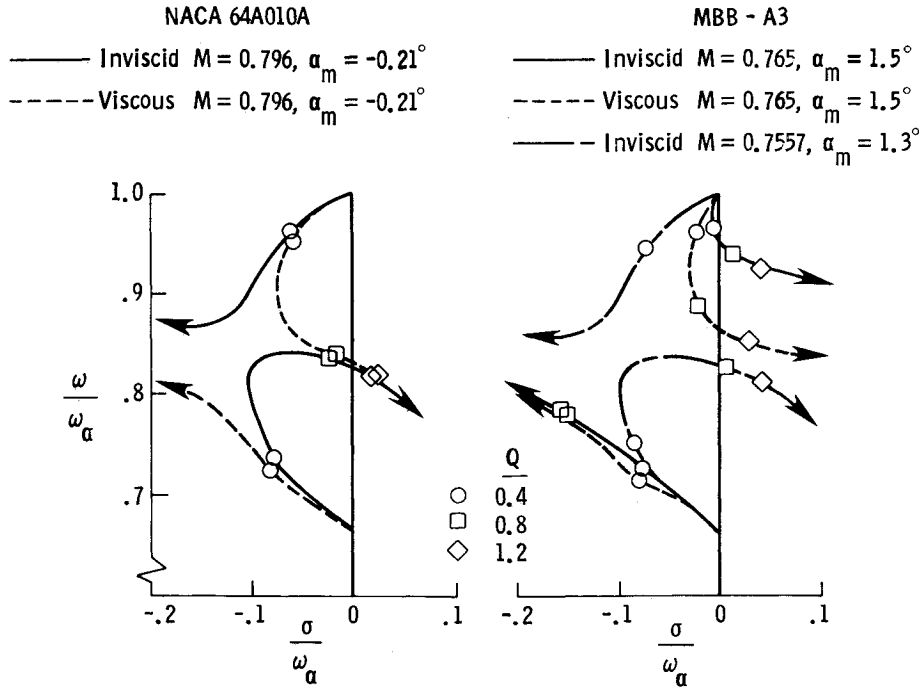

Fig. 11 Effects of viscosity on Padé model dynamic pressure root loci of Example 2.

Concluding Remarks

Viscous effects on transonic airfoil stability and response have been investigated based on the use of the XTRAN2L transonic small-disturbance code. Aerodynamic calculations including viscous effects were performed using an integral boundary-layer model coupled to the inviscid potential outer flow in a quasi-steady fashion.

Transonic unsteady aerodynamic coefficients required for stability calculations were computed using a pulse transfer-function analysis. Excellent agreement was found between the pulse transfer function and oscillatory airloads, thus demonstrating the ability of the pulse analysis to include viscous effects. Inviscid and viscous pulse results showed the same trends with respect to reduced frequency, although differences occur for low values of k. Viscous pulse computations showed better overall agreement with experimental data than the inviscid pulse computations.

Nonlinear time-marching flutter solutions were obtained which showed the effects of viscosity and amplitude on airfoil response behavior and flutter. A two degree-of-freedom (plunge and pitch) aeroelastic system was considered. Representative responses for the NACA 64A010A airfoil were presented for two different example sets of aeroelastic parameter values. In both examples, the viscous responses at flutter had the same characteristics as the inviscid responses including very similar amplitudes. In the first example, which had normal modes similar to those of a streamwise section near the tip of a swept-back wing, large increases in flutter dynamic pressure Q_F resulted with the inclusion of viscous effects. In the second example, which had normal mode frequencies that were close together, viscosity had little effect on Q_F.

Aeroelastic stability analyses were performed using a Padé state-space aeroelastic model. Dynamic pressure root-loci were presented for the NACA 64A010A and MBB-A3 airfoils for the two example sets of aeroelastic parameter values. For the first example considered, the Padé model root-loci showed that viscous effects increased damping in the bending mode, thus delaying the onset of flutter. Changes in flutter dynamic pressure were correlated with changes in steady shock strength and location. Inclusion of viscous effects weakened the shock on the MBB-A3 airfoil more than that of the NACA 64A010A airfoil and consequently caused larger increases in Q_F. For the three sets of computations performed for the MBB-A3 airfoil, decreased shock strength and forward shock displacement produced increased Q_F values. The most accurate aeroelastic calculations result when the steady pressure distributions compare closest with experimental data. These results emphasize the need to accurately predict steady shock strength and location because of the sensitivity of the aeroelastic behavior to these parameters. In general, the Padé model root-loci were in good overall agreement with the time-marching damping and frequency estimates in both the inviscid and viscous cases. In the second example, viscosity caused an insignificant change in the NACA 64A010A flutter dynamic pressure. For the MBB-A3 airfoil, a 66% increase in Q_F resulted with the inclusion of viscous effects which was attributed to a stronger steady shock in comparison with the NACA 64A010A airfoil. Padé model flutter dynamic pressure values for both example sets of aeroelastic parameter values were typically nonconservative.

Acknowledgments

This work constitutes a part of the first author's M.S. thesis at Purdue University and was supported by the NASA Langley Graduate Aeronautics Program under Grant NAG-1-372.

References

[1]Ballhaus, W. F., "Computational Aerodynamics and Supercomputers," NASA TM 85887, Jan. 1984.

[2]Ballhaus, W. F. and Goorjian, P. M., "Implicit Finite-Difference Computations of Unsteady Transonic Flow about Airfoils," *AIAA Journal*, Vol. 15, Dec. 1977, pp. 1728-1735.

[3]Rizzetta, D. P., "Procedures for Computation of Unsteady Transonic Flows Including Viscous Effects," NASA CR 166249, Jan. 1982.

[4]Guruswamy, P. and Goorjian, P. M., "Effects of Viscosity on Transonic-Aerodynamic and Aeroelastic Characteristics of Oscillating Airfoils," *Journal of Aircraft*, Vol. 21, Sept. 1984, pp. 700-707.

[5]Houwink, R., "Results of a New Version of the LTRAN2-NLR Code (LTRANV) for Unsteady Viscous Transonic Flow Computations," National Aerospace Laboratory, the Netherlands, NLR TR 81078U, July 1981.

[6]Houwink, R. and van der Vooren, J., "Improved Version of LTRAN2 for Unsteady Transonic Flow Computations," *AIAA Journal*, Vol. 18, Aug. 1980, pp. 1008-1010.

[7]Howlett, J. T., "Efficient Self-Consistent Viscous-Inviscid Solutions for Unsteady Transonic Flow," AIAA Paper 85-0482, Jan. 1985.

[8]Whitlow, W. Jr., "XTRAN2L: A Program for Solving the General Frequency Unsteady Transonic Small Disturbance Equation," NASA TM 85723, Nov. 1983.

[9]Seidel, D. A., Bennett, R. M., and Whitlow, W. Jr., "An Exploratory Study of Finite-Difference Grids for Transonic Unsteady Aerodynamics," AIAA Paper 83-0503, Jan. 1983 (also NASA TM 84583, Dec. 1982).

[10]Edwards, J. W. Bennett, R. M., Whitlow, W., Jr., and Seidel, D. A., "Time Marching Transonic Flutter Solutions Including Angle of Attack Effects," *Proceedings of AIAA/ASME/ACHE/AHS 23rd Structures, Structural Dynamics and Materials Conference,* AIAA, New York, May 1982, pp. 220-233.

[11]Bennett, R. M. and Desmarais, R. N., "Curve Fitting of Aeroelastic Transient Response Data with Exponential Functions in Flutter Testing Techniques," NASA SP-415, 1975, pp. 43-58.

[12]Batina, J. T. and Yang, T. Y., "Application of Transonic Codes to Aeroelastic Modeling of Airfoils Including Active Controls," *Journal of Aircraft*, Vol. 21, Aug. 1984, pp. 623-630.

[13]Batina, J. T. and Yang, T. Y., "Transonic Calculation of Airfoil Stability and Response with Active Controls," *Proceedings of the AIAA/ASME/ACHE/AHS, 25th Structures, Structural Dynamics and Materials Conference,* AIAA, New York, May 1984, pp. 578-588; (also NASA TM 85770, March 1984).

[14]Bland, S. R., "AGARD Two-Dimensional Aeroelastic Configurations," AGARD-AR-156, Aug. 1979.

[15]Davis, S. S., "NACA 64A010 (NASA Ames Model) Oscillatory Pitching," *Compendium of Unsteady Aerodynamic Measurements,* AGARD Rept. 702, Aug. 1982.

[16]Bucciantini, G., Oggiano, M. S., and Onorato, M., "Supercritical Airfoil MBB-A3, Surface Pressure Distributions, Wake and Boundary Condition Measurements," AGARD-AR-138, May 1979, pp. A8-1—A8-25.

[17]Isogai, K., "Numerical Study of Transonic Flutter of a Two-Dimensional Airfoil," National Aerospace Laboratory, Tokyo, Japan, Rept. NAL TR-617T, July 1980.

[18]Houwink, R., "Unsteady Transonic Flow Computations for AGARD 2-D Aeroelastic Configurations," National Aerospace Laboratory, the Netherlands," NLR Memo AE-83-004 U, March 1983.

[19]Bland, S. R. and Edwards, J. W., "Airfoil Shape and Thickness Effects on Transonic Airloads and Flutter," *Journal of Aircraft,* Vol. 21, March 1984, pp. 209-217.

[20]Howlett, J. T., Private Communication, April 1, 1986.